Supplementary Materials for

Femtosecond Structural Dynamics Drives the *Trans/Cis* Isomerization in Photoactive Yellow Protein

Kanupriya Pande, Christopher D. M. Hutchison, Gerrit Groenhof, Andy Aquila, Josef S. Robinson, Jason Tenboer, Shibom Basu, Sébastien Boutet, Daniel P. DePonte, Mengning Liang, Thomas A. White, Nadia A. Zatsepin, Oleksandr Yefanov, Dmitry Morozov, Dominik Oberthuer, Cornelius Gati, Ganesh Subramanian, Daniel James, Yun Zhao, Jake Koralek, Jennifer Brayshaw, Christopher Kupitz, Chelsie Conrad, Shatabdi Roy-Chowdhury, Jesse D. Coe, Markus Metz, Paulraj Lourdu Xavier, Thomas E. Grant, Jason E. Koglin, Gihan Ketawala, Raimund Fromme, Vukica Šrajer, Robert Henning, John C. H. Spence, Abbas Ourmazd, Peter Schwander, Uwe Weierstall, Matthias Frank, Petra Fromme, Anton Barty, Henry N. Chapman, Keith Moffat, Jasper J. van Thor, Marius Schmidt

correspondence to: m-schmidt@uwm.edu

This PDF file includes:

Materials and Methods
Supplementary Text
References 48-86
Figs. S1 to S12
Tables S1 to S5

Materials and Methods

Sample preparation, data collection

PYP micro-crystals were grown and SFX data were collected as previously described (*25*). Microcrystals were injected using a liquid jet injector (*48*). X-ray data were collected on a Cornell Stanford Pixel Area Detector (*49*) located at a nominal distance of 84 mm from the jet. An electronic low gain mask was used to 4.5 Å resolution to increase the dynamic range of the detector by a factor ~6. 40 fs X-ray FEL pulses (9.5 keV, 2 mJ/pulse) were focused to 1 µm.

Laser excitation and timing

10 µJ of 450 nm pulses were generated using an TOPAS-prime pumped by a 800 nm CPA Ti:sapph system (Coherent Legend). These were focused onto the jet using a f=+300mm lens to give a 140(±10) µm (FWHM) spot corresponding to an energy density of 0.75 mJ mm^{-2}. Due to `hot-spotting' in the output of the TOPAS, it was necessary to install a telescope to expand the beam prior to focusing in order to achieve the required power density. The telescope consisted of two AR coated lenses (f= -70 mm and +200 mm). When combined with the f=+300mm lens, the 40±5 fs TOPAS output pulses were stretched to 140±5 fs. The on-axis configuration ensures a stable laser beam position. We determined the exact laser pulse shape and pulse duration after all the optical components using Second Harmonic Generation Frequency Resolved Optical Gating (SHG-FROG), which was installed by the Imperial College team at the beamline (see further below).

The highest laser power that could excite as many molecules as possible without generating significant laser damage was determined spectroscopically beforehand using laser pulses of 100 fs, 300 fs and 1 ps duration (see below) (*50*). Optimally, a 7% - 10% photoactivation yield was reached with positively chirped 100 fs laser pulses directly on resonance and energy densities up to 0.8 mJ/mm^2; single-shot photo-bleaching did not exceed 0.5% (*50*). For spatial alignment of the laser and X-ray FEL beams, the overlap was adjusted visually using a YAG screen. Time zero (T0) was determined by pumping a YAG screen at the interaction plane with the X-rays and measuring the change in the transmission of the optical laser as a function of delay between the two pulses. This determined T0 to an accuracy of < 150 fs. The nominal pump-probe time delay Δ_{set} could then be set by offsetting the laser pulse timing relative to the X-ray pulses. To correct for the pump-probe jitter Δ_{jitter} of individual pulses, a timing tool was used upstream of the vacuum chamber. By changing the phase delay between the laser oscillator and an accelerator RF reference signal, the 140 fs laser pulse could be precisely adjusted to any selected pump-probe delay. Δ_{jitter} measured by the timing tool was added to the selected time delay Δ_{set}. Larger time drifts between the FEL X-ray pulses and laser pulses occurred over the duration of data collection. These drifts could be *measured* by changing the delay line of the timing tool, or *corrected* by changing the laser offset. Correction was preferred since this method left Δ_{set} unchanged, thus simplifying subsequent timing analysis. Once the traces were detected again by the timing tool, Δ_{jitter} was directly accounted for. If the drift was not corrected, it had to be added to the time-delay Δ_{set}. Since we acquired data both with and without correction, our temporal density of diffraction patterns (snapshots) was skewed (Fig. S1). As a consequence, when sorting into timing bins containing equal numbers of patterns, the time axis was not sampled at equal intervals (Fig. S1). Jitter correction was done for all diffraction patterns in the fs time range. For the 3 ps and the 7200 ns delays, the jitter was less than 10% of the time delay and could therefore be disregarded.

Data Binning, Common Scale

For the positive control, data with a pump probe time-delay of 200 ns were collected. Reference (dark) data were collected at 120 Hz in a separate data set at a -1 ps time delay i.e. the

X-ray pulse arrives before the laser pulse. The negative time delay was intended to account for potential effects of the intense fs blue laser stray light on the detector response. The fs time-range was covered by 2 nominal delays, 300 fs and 600 fs. Data were collected in the following order: First, 1.9 x 10^6 snapshots with a nominal delay of 200 ns were collected within 6 h. Then 3.3 x 10^6 snapshots with a nominal delay of 600 fs were collected for 13 h followed by collecting 1 x10^6 snapshots for the -1 ps reference dataset for 3 h. We continued to collect 1.6 x 10^6 snapshots with a 600 fs nominal delay for 8 h, and 1.4 x 10^6 snapshots with a delay of 3 ps for 7 h. Finally we collected 1.5 x10^6 snapshots with a nominal delay of 300 fs for 8 h. This arrangement is necessitated by the fact that the laser cannot be switched at 120 Hz between the nominal pump probe delays Δ_{set} that we wished to use of 300, 600 and 3 ps. If we were able to achieve this switching and to add a fourth delay of -1 ps (dark), the combination of fast switching of Δ_{set} with the delay jitter would have resulted both in a more uniform distribution of diffraction patterns with time delay than that achieved (Fig. S1), and in the association of each group of four delays with its own dark pattern, close in clock time. However, the fact that LCLS patterns are each obtained on a new crystal means that interleaving of dark and light patterns offers much less reduction in systematic errors than in the synchrotron case, where dark and light data are collected on the same crystal, close in clock time. In total we collected 10.3 x 10^6 detector readouts (snapshots) within 45 hours spread across five 12 h shifts. 9.4 x 10^5 snapshots (9.1 %) were hits and 6 x 10^5 (5.8 %) could be indexed (see also Tab. S1 for statistics).

To cover the fs and early ps time range, these three nominal pump probe delays Δ_{set} were used. Individual diffraction patterns (snapshots) containing Bragg reflections were designated as hits and selected using Cheetah (*51*). The timing tool information was used to determine corrections to Δ_{set} for each snapshot by locating the pulse-to-pulse transition edge in the time tool signal and converting this to a delay time. This resulted in a continuous distribution of delay times (Fig. S1). All hits were indexed and integrated using CrystFEL version 0.6.1 (*52, 53*). The highly partial intensities from all time-delays, around 500,000 indexed patterns in total (Tab. S1), were merged to obtain an average dataset. The indexing ambiguity was solved at this stage for all diffraction patterns together, as previously reported (*25*). The intensities were merged using the ‘partialator’ from CrystFEL (version 0.6.1+ab098ce1), applying individual linear and Debye-Waller scaling factors to each crystal to best fit the merged data in an iterative procedure. Partialities were not assigned. Diffraction patterns were scaled in one large scaling job to ensure that intensities from all diffraction patterns and all time delays were on the same scale. The indexed snapshots were finally merged into 16 bins with around 20000 snapshots each, spanning the time range from ~100 fs to 1.1ps (Fig. S1, red squares, and Tab. S1A); or into 8 bins (Tab. S1B); or into two bins (Tab. S1C).

Difference maps and Singular Value Decomposition

Difference maps and structural models are displayed by ‘UCSF-CHIMERA’ (*54*) throughout the manuscript. Difference structure factor amplitudes and weighted DED maps were calculated from the SFX amplitudes for each of the 16 time delays (Tab. S1A) as described(*25*) using the SFX data of the -1 ps negative time delay as the dark reference. Following visual inspection of the DEDs in 8 bins, the DED_t in 16 bins (thus offering better time resolution) were subject to singular value decomposition (*32*), solely to pin-point the time when the structural transition occurs. The volume of the asymmetric unit subjected to SVD was determined by the pCA chromophore atoms, the Cys69 sulfur and the Glu46 carboxyl. We did not attempt any interpretation of the singular vectors in terms of structure and/or kinetic models. Fig. S2B shows the result of the SVD analysis.

The time evolution of the overall signal in the DEDs is represented by the first right singular vector (rsv1, black circles). It shows how the total difference electron density evolves as a function of time from relatively small values around 100 fs to larger values on longer fs and ps time scales. The time course of rsv1 can be fitted empirically by a simple exponential function of the form

$$rsv1(t) = A_1 + B_1\left[1 - exp\left(\frac{t}{\tau_1}\right)\right]. \qquad \text{(S1)}$$

The signal in the DED maps rises with τ_1=155 fs; larger structural displacements persist to the largest time delay studied, 3 ps. The dashed blue and red curves in Fig. S2B were calculated also by eqn. S1, by re-interpreting the deviations from the fitted curve. The second right singular vector (rsv2, red squares), shows a pronounced variation with time. It was fit by an additional empirical function to determine the time delay at which this variation occurred τ_{ct}:

$$rsv2(t) = \frac{A_2}{1+exp\frac{t-\tau_{tc}}{B_2}}\,. \qquad \text{(S2)}$$

Note that Eqns. S1 and S2 are purely empirical and have no physical (predictive) power. The transition time τ_{tc} is about 550 fs. This is consistent with our earlier observation that on the fast fs time scale < 500 fs the difference maps (DED_{fast}) are qualitatively different from those (DED_{slow}) on the longer fs time scales > 700 fs (Fig. 2 and Fig. S9). The derivative of eqn. S2 is a bell-shaped curve whose full width half maximum (FWHM) depends on the fit parameter B_2. After fitting eqn. S2 to rsv2, parameter B_2 is ~50 fs and the FWHM of the derivative of eqn. S2 is ~180 fs (Fig. S2B, blue curve).

Refinement and Phased Difference Maps

200 ns pump-probe delay as positive control and reference model.

The dark (reference) model (PYP_{ref}) was refined against the SFX structure factor amplitudes to 1.5 Å resolution (see above). To refine a model at the 200 ns pump-probe delay, we first inspected the difference map DED_{200ns}. This map arises from a mixture of two structures, pR_1 and pR_2, available from Protein Data Bank (*55*) entries 4WLA and 4WL9, which were used as a starting model. The CCP4 (*56*) program 'REFMAC5' (*57*) was used to refine the structure (Tab. S2). The pCA chromophore was identified from the 'HC4.cif' library, and linked to cysteine using the program 'JLIGAND'. This construct was used then as an unusual amino acid in the refinement, with the advantage of offering full control over the restraints. The pR_1 and pR_2 models were refined against extrapolated structure factor amplitudes $|F^{ext}| = |F^{c,dark}| + n \times w\Delta F$ where wΔF are weighted difference structure factor amplitudes (between the 200 ns time delay and the reference) and n was 10, with the same restraints used to refine the dark model. Fig. 1C in the main text presents the refined 200 ns structure superimposed on the DED_{200ns} map.

3 ps and below.

On the ultrafast time scales (fs and ps), structural refinement was challenging. There are only limited diffraction data and any refined structures will be far from equilibrium (see main text). The goal of refinement is to obtain chemically and structurally plausible chromophore configurations that account for the most significant positive (features β and γ in Fig. 2) and negative difference density (features α in Fig. 2) around the chromophore. There is an obvious difference in the DED maps between the 3 ps delay and the fast fs time points (compare Fig. 2A-B with Fig. 2E). At 3 ps the positive DED that corresponds to the double bond is aligned along the axis of the chromophore tail (dashed line in Fig. 2E, and Fig. S12C), whereas on the fast fs time scale this feature is at an angle with the tail (dashed line in Fig. 2A, and Fig. S12A). The chromophore tail structures on the fast fs time-scale clearly differ from those at 3 ps. To derive the restraint for the C_1-C_2=C_3-$C_{1'}$ torsional angle (ϕ_{tail}), we rely on guidance by quantum molecular mechanics (QM/MM) computer simulations (see below). A trajectory ϕ_{tail} is shown in Fig. S7. On the fast fs time scale this angle is > 100 deg, which corresponds to a twisted *trans* configuration. However, at longer time scales, this angle is close to 0^o, which corresponds to a full *cis* configuration. In order to minimize bias towards the QM/MM simulations, we did not make use of the QM/MM force-field for our refinement, but accepted the torsional angle from the QM/MM calculations as a restraint to guide and corroborate our structural analyses.

Refinement of the 3 ps structure.

To refine a structure and to explain the features in the 3 ps difference map (DED_{3ps}), we restrained ϕ_{tail} to the QM/MM value of about 20^o (Fig. S7C). Extrapolated structure factor amplitudes $|F^{ext}|$ were calculated as above (for the 200 ns time point) by adding the observed (measured) weighted differences structure factor amplitudes ($w\Delta F^{obs}$) to calculated structure factors ($F^{c,dark}$) derived from the refined reference (dark) structure: $|F^{ext}| = |F^{c,dark}| + n \times w\Delta F$. Initially n = 11. The initial model was refined to $|F^{ext}|$ and a new model obtained. ϕ_{tail} observed in this new model is ~70^o. New structure factors F^{light} with amplitudes and phases were calculated from this model. Difference phases $\phi^{\Delta F,calc}$ were calculated by subtracting $F^{c,dark}$ from $F^{c,light}$. $\phi^{\Delta F,calc}$ were combined with $w\Delta F^{obs}$ and phased, weighted difference structure factors $w\Delta F^{obs,\phi}$ were obtained. New extrapolated structure factors $F^{new} = F^{c,dark} + n \times w\Delta F^{obs,\phi}$ were calculated, this time by adding $nw\Delta F$ as a vector in the complex plane. The value of n was increased to 17. A new model was refined against $|F^{new}|$ and the procedure iterated until convergence, when ϕ_{tail} settled at ~35^o. A difference map calculated from ΔF^{calc} obtained by subtracting structure factors of the reference model from those of the final model essentially reproduces the observed DED features. Importantly, the more parallel alignment of the difference feature β1 in Fig. 2E is reproduced. The configuration of the chromophore in this structure (PYP_{3ps}) is *cis* (Tab. S2).

Refinement of structures on the fs time scale.

For the refinement on the fs time-scale the X-ray data were sorted into bins containing ~40,000 patterns, each (Tab. S1B). Up to the 455 fs bin, the strongly kinked positive feature β1 (see Figs. 2, S9 and S12A) indicates a *trans* configuration. ϕ_{tail} was restrained to the QM/MM value of 120^o. At times larger than 700 fs the DED maps and features β1 are similar to that at 3 ps (compare Fig. 12, B and C), and ϕ_{tail} was restrained to 20^o. Refinement commenced as described above. Fig. 3C and Tab. S3 show the resulting torsional angles. At times faster than 500 fs, the chromophore adopts a *trans* configuration, after 700 fs the configuration is *cis*. We could not successfully refine a single model into the 699 fs DED map time bin presumably because it arises from a mixture of *trans* and *cis* configurations which our data are inadequate to resolve. ϕ_{tail} determined at various time delays follows the time course derived by singular value decomposition (compare Fig. S2 A-B). A transition time τ_{tc} of 590 fs was obtained by fitting eqn. S2 to the ϕ_{tail}. In order to enhance the signal to noise ratio of the data and the credibility of the structures we then sorted our data in even larger bins (Tab. S1C).

The DED map determined from X-ray data in the 100-400 fs bin (81327 indexed diffraction patterns, Tab. S1C) is shown in Figs. 3A and S9B. For refinement of the corresponding structure PYP_{fast}, ϕ_{tail} was restrained to the QM/MM value of 120^o as for the fast time delays above. Upon convergence of the refinement, ϕ_{tail} settled at 140^o. Feature β1 that aligns across the tail axis (Fig. 2A, dashed line) is exactly reproduced (see also Fig. S12A). Clearly, the configuration of the chromophore is *trans*. On time-scales > 550 fs a transition to the *cis* configuration occurs (Fig. 2D-F, Fig. 3B and Fig. S9C-D). The last three time bins were combined to further boost the signal to noise ratio in the DED map (Tab. S1C, 800-1200fs bin, 157082 indexed patterns). The result is shown in Fig. 3B and Fig. S9D. Feature β1 largely determines the configuration of the double bond. β1 is more aligned along the tail axis (compare Fig. 2E, dashed line). The positive feature β3 in Fig. S9D indicates a shift in the ring-phenolic oxygen. As a result (Fig. 2D-F), the ring shifts and the hydrogen bond to Glu46 is broken (3.7 Å). ϕ_{tail} is around 50°, close to that of the 3 ps structure (40°). Fig. S3 shows a schematic view of the *trans* to *cis* transition that involves this structure. Overall, on the longer fs time scale the structure PYP_{slow} is already *cis* but further relaxation towards PYP_{3ps} is yet to occur. Notably, the hydrogen bond to Glu46 is re-established at 3 ps. With these structures at hand, the *trans* to *cis* isomerization can be structurally understood by concerted rotations about the C_1-C_2 and the C_3-$C_{1'}$ single bonds as well as the C_2=C_3 double bond as outlined in Fig. S3.

Overall, the refinement is robust and does not rely heavily on the QM/MM torsional angle restraints. Indeed, the models were reproduced with a variety of starting torsional angles ϕ_{tail} and ϕ_{tail} restraints. For example the 455 fs model (Fig. 2C, with ϕ_{tail} = 145°) is reproduced using either 0° or 180° for the initial torsional angle and 90° (the QM/MM value right before the hop, Fig. S7) or 180° as weak torsional restraints. Similarly, the 455 fs model (which is *trans*) can be used as a starting model to reproduce the 3 ps model (which is *cis*, ϕ_{tail}=35°). Note: B-factors refined against extrapolated amplitudes are not reliable partly because the time-dependent X-ray data are scaled against the reference (dark) data and partly because the differences amplitudes are added to the dark structure factors using dark state model phases rather than their true (but unknown) phases. For more information on phases of difference structure factors, see Schmidt 2008 (*58*).

Difference-difference (residual) maps.

Most importantly, the principal difference electron density features are faithfully reproduced by difference maps calculated from the refined models. To obtain residual maps, difference maps calculated from the refined models ($|F^{calc}(t)|-|F^{calc}(dark)|$ difference maps) were subtracted from the observed weighted $|F^{obs}(t)|-|F^{obs}(dark)|$ difference maps. The resulting difference-difference maps are shown in Fig. S10. The absence of strong signal in residual maps shown in Fig. S10A-B,F indicates a match between the model structure and the observed difference density. Conversely, the presence of strong features in residual maps where a wrong model was deliberately used confirms the inadequacy of that model (Figs S10C-E).

Structural Comparison, Volumes, Radius of Gyration, Energies.

The PYP structures refined here were compared with structures from the literature (PDB-codes 4I38, 4B90, 1TS0; see Tab. 1). Local structural changes were determined by averaging the distances between equivalent chromophore atoms of the dark structure and those at each time delay Δt using Coot (*59*). Global structural changes were determined by averaging the $C_\alpha - C_\alpha$ distances of equivalent residues of the dark and the structures at each time-delay Δt using 'lx_lsqman' (*60*) (Tab. S4). For protein volume determination a water accessible surface (*61, 62*) must be calculated (Fig. S4). The water accessible surface and the PYP volume were determined by a probe of 1.5 Å radius using the 'volume assessor' located at http://3vee/molmovdb.org/volumeCalc.php (*63*). The radius of gyration of PYP was calculated by the standard equation (eqn. S3) (*64*).

$$R_g^2 = \sum_i m_i(\vec{r}_i - \vec{r}_c)^2 / \sum_i m_i, \tag{S3}$$

where R_g^2 is the square of the radius of gyration, m_i is the mass of atom i, $\vec{r}_i$ is the coordinate of atom i, and $\vec{r}_c$ is the center of mass of the PYP molecule. Results are listed in Tab. 1.

The structural displacements for 9 carbon, 2 oxygen and 7 hydrogen atoms of the chromophore (147 g/mol) are <0.7 Å> on the average after 250 fs. Using the classic equation $s = \frac{1}{2}at^2$, the acceleration must have been 2 x 10^{15} m/s^2. The final velocity (starting with v=0) is $v = at = 500\,\frac{m}{s}$. The force on the chromophore is accordingly $F = \frac{0.147kg/mol}{A} \cdot 2x10^{15}\,\frac{m}{s^2} = 4.88x10^{-10}N$ or ~500 pN, with A the Avogadro number (6.022 x 10^{23} N/mol). The energy is the force times the displacement which gives 3.2 x 10^{-20} J or 0.2 eV (same result is obtained when the kinetic energy is considered with v = 500 m/s).

Supplementary Text

Spectroscopic investigations on crystals to determine the maximum permissible laser power.

Spectroscopic investigations were performed on thin (2 – 3µm) crystalline material produced by squeezing a large PYP crystal between two cover slides (*65*). 900 fs, 300 fs and 100 fs laser pulses with varying energy density were used to start the photocycle. The spectra were probed after the laser pulse with a fast spectrometer (Fig. S5A-B; 180 µs time delay) or with a continuous wave laser source and photodiode detector (Fig. S5C-D; 1 ms time delay). Irreversible bleaching is an indication for damage (Fig. S5A). The percentage of molecules that could be brought into the photocycle without (or with only small) irreversible bleaching was up to 10% (*50*). Power densities up to 0.8 mJ/mm^2 could be used with positively chirped 140 fs pulses, while keeping single-shot photobleaching below 0.5%.

FROG Measurements.

The 450 nm laser pulses were characterized using a custom built SHG-FROG setup (*27*). A schematic of the device is shown in Fig. S6A. A beam splitter was used to split the 450 nm pulse into two replicas which were sent on two independent delay lines. One line had a motorized delay stage to control the temporal delay (τ) between the two pulses. In order to reduce the amount of dispersion introduced by the FROG setup itself, the beamsplitter was a 2 µm thick pellicle (Thorlabs BP245B1) and focusing was performed using reflective optics. The replicas were focused into a 20 µm substrate mounted BBO crystal (θ= 55°, φ = 90°) (Mesaphotonics) which was inclined at about 13° to phase match SHG at 450 nm. When spatially and temporally overlapped in the crystal, it is possible for SHG to result from the conversion of one photon from each replica pulse. Due to the non-collinear geometry and momenta cancellation, this 225 nm signal ($I_{SHG}(\omega\tau)$) is emitted on axis and easily separated from the fundamentals; it was measured using a custom-modified UV spectrometer. When recorded as a function of relative delay, this FROG signal can be written as

$$I_{SHG}(\omega\tau) = \int I(t)I(t+\tau)e^{-i\omega t}. \tag{S4}$$

When plotted as a function of spectra and delay this produced a "FROG trace" (Fig. S6B) which was analyzed using the FROG code software package (J.Wong et al. http://frog.gatech.edu/). This program creates a theoretical FROG trace (Fig. S6C) using a test pulse and then iteratively alters the simulated pulse parameters to produce the best fit of the replicated to the experimental trace. When fitting is achieved below a suitable error, the algorithm provides full reconstruction of the pulse's spectral and temporal profile including phase. It is also possible to recover the second order dispersion or group delay dispersion (GDD) and third order dispersion (TOD) by fitting a 3rd order polynomial to the spectral phase. Phases associated with spectral intensities smaller than 1/e of the maximum intensity were ignored as they have little meaning and are mostly artifacts of the fitting. The FROG reconstruction of the pulses that were used to pump the PYP crystals is shown in Fig. S6D-E. The pulses were found to be 140±5 fs long with a GDD of $\approx$1000 fs^2 and TOD $\approx$+1300 fs^3. The large dispersion was expected due to the 8 mm of BK7 and 4 mm of fused silica in the beam path. Since the measured GDD for the un-stretched TOPAS output was less than +50 fs^2, the GDD of $\approx$1000 fs^2 is very close to literature value for glass introduced ($\approx$+1100 fs^2).

Our positively chirped laser pulses favor the generation of the non-stationary excited state (*28*), hence optimizing the quantum yield of the reaction. Ultrafast spectroscopy literature is in good agreement with the time-dependence of the dynamics observed here. The on-resonance excitation and sign and magnitude of second order dispersion minimizes non-linear cross-sections of excited state absorption and stimulated emission (*5, 66-68*). While maximizing S_0 to S_1 population transfer, the intense femtosecond pulse also generates vibrational coherence(*41*). Ultrafast vibrational spectroscopy on PYP has established the chromophore response on ultrafast time scale (*42*). Using femtosecond stimulated Raman spectroscopy, a Franck-Condon (FC) intermediate is observed at ~100fs (*42*), distinct from the major S_1 decay process with a ~450 fs time constant. The FC state already shows chromophore distortions. The decay of this FC state with a ~ 170 fs time constant agrees with the structural changes seen in our experiment prior to excited state decay, occurring with ~ 450 fs time constant. Furthermore, the chromophore tail carbonyl out-of-plane vibration downshifts from 665 to 640 cm^{-1} concurrent with excited state decay which was interpreted as resulting from motion along the photo-isomerization coordinate (*42*).

QM/MM Calculations

Chromophore force field

All interactions were modeled with the Amber03 force field (*69*). Bonded and Lennard-Jones parameters to model the chromophore were determined based on the similarity of the chromophore atoms to the atoms already defined in the force field. Equilibrium bond lengths and angles were taken from an optimized chromophore model in vacuum (deprotonated thiomethyl p-coumaric acid, TMPCA). The optimization was performed at the B3LYP/6-31G(d) level of Density Functional Theory(*70, 71*) with the Gaussian09 program (Gaussian, Inc., Wallingford). The partial charges of the atoms were derived following the procedure recommended for the Amber03 force field (*69, 72*). First, the geometry of TMPCA was minimized at the HF/6-31G** level of *ab initio* theory. To account for the effect of a protein environment in these calculations, the IEFPCM continuum solvent model(*73*) was used with a relative dielectric of 4.0.(*69*) After geometry optimization, the electrostatic potential at 10 concentric layers of 17 points per unit area around each atom was evaluated using the electron density calculated at the B3LYP/cc-pVTZ level of theory, again using the IEFPCM continuum solvent model with a relative dielectric of 4.0. The atomic charges were obtained by performing a single-stage RESP fit to the electrostatic potential without symmetry constraints (*72*). The recommended two-stage fit with symmetry constraints on the phenol ring was considered unnecessary, because a high rotation barrier prevented sampling configurations with a flipped phenol ring in our classical MD simulations. Also, the non-symmetric charge distribution of the phenol ring yielded a more accurate fit to the quantum mechanical electrostatic potential than the symmetrized distribution.

Molecular dynamics simulation setup.

The starting coordinates of the PYP crystal were taken from the x-ray structure (PDB entry: 2ZOH) (*74*). Six copies of the protein, including 120 crystal waters, were placed inside the unit cell with periodic boundaries and soaked in 5M NaCl solution by adding 909 TIP3P waters (*75*), 59 Na^+ and 23 Cl^-. The total system contained 16,553 atoms and was simulated classically for 100 ns. The classical MD simulations were run at constant volume and temperature of 300 K (*76*), with a time constant of 0.1 ps for the temperature coupling. The LINCS algorithm was used to constrain bond lengths (*77*), allowing a time step of 2 fs in the classical simulations. SETTLE was applied to constrain the internal degrees of freedom of the water molecules (*78*). A 1.0 nm cut-off was used for non-bonded Van der Waals' interactions, which were modeled by Lennard-Jones potentials. Coulomb interactions were computed with the smooth particle mesh Ewald method(*79*), using a 1.0 nm real space cut-off and a grid spacing of 0.12 nm. The relative tolerance at the real space cut-off was set to 10^{-5}. All force field simulations were performed in single precision with the Gromacs-4.5.3 molecular dynamics program (*80*).

In the excited state dynamics simulations the QM subsystem, which included part of the backbones of Pro68, Cys69, the sidechains of Tyr42, Glu46 and Cys69, and the *p*CA chromophore (Fig. S7) in one of the asymmetric protein units, was described at the CASSCF/cc-pVDZ level (*81*), with an active space of 12 electrons and 11 orbitals, *i.e.*, the complete π-system of the chromophore. Surface hopping was used to model the excited state decay. As explained elsewhere (*82*), hops are triggered when the quantum mechanical probability for a transition from S_1 to S_0 equals unity, which can only occurs when the classical trajectory hits the conical intersection hyper-line. Although such strict hopping criterion could underestimate hopping (*83*), we consider this an advantage if only a few trajectories can be computed. An additional advantage of our *diabatic* surface hopping approach is that we obtain structural information about the location of the S_1/S_0 seam in the protein. The remainder of the system, consisting of the apo-protein, 1,629 TIP3P water molecules (*75*), 23 Cl^- and 59 Na^+ ions in the periodic unit cell, was modeled with the AMBER03 force field (*69*). The five bonds connecting the QM and MM subsystems were replaced by constraints (*77*) and the QM part was capped with hydrogen atoms. The force on the cap atoms was distributed over the two atoms of the bond. Because the QM subsystem was mechanically embedded into the MM system (Fig. S7A), electrostatic and Lennard-Jones interactions between MM and QM atoms were added. The time step was reduced to 1 fs. Photon absorption was modeled as an instantaneous, on-resonance transfer of the system from the electronic ground state surface (S_0) to the first singlet excited state (S_1) potential energy surface.

Prior to the excited state non-adiabatic QM/MM MD simulations, the system was simulated at the MM level for 100 ns. From this 100 ns trajectory, three snapshots were randomly selected and further equilibrated for 5 ps at the QM/MM level, using the Restricted Hartree-Fock (RHF) method to model the electronic wave function of the QM subsystem (Fig. S7A). All QM/MM simulations were performed with the QM/MM interface between (*80*) and Firefly version 8.1.0 (*84*).

Photo-isomerization trajectory.

The main results of the simulations are summarized in Tab. S5. In all three simulations the primary photo-dynamics initiated by photon absorption involves a rapid rotation of the C_2=C_3 torsion into a 90° twisted S_1 minimum (Fig. S7B, Fig. S8). After a short period in this S_1 minimum, the system reaches the nearby S_1/S_0 conical intersection seam and decays to the electronic ground state (S_0) surface. Back on the ground state surface, the chromophore continues isomerizing towards the *cis* conformation (a, c, Tab. S5). During this process, the hydrogen bond between the carbonyl of the chromophore (O_1) and the backbone amino group of Cys69 (N) remains intact (Fig. S7B, Fig. S8). The chromophore may relax also into the *trans* configuration, restoring the dark state of the protein. The number of trajectories is statistically small, but yield a consistent mechanism that is also in full agreement with previous simulations (*20*).

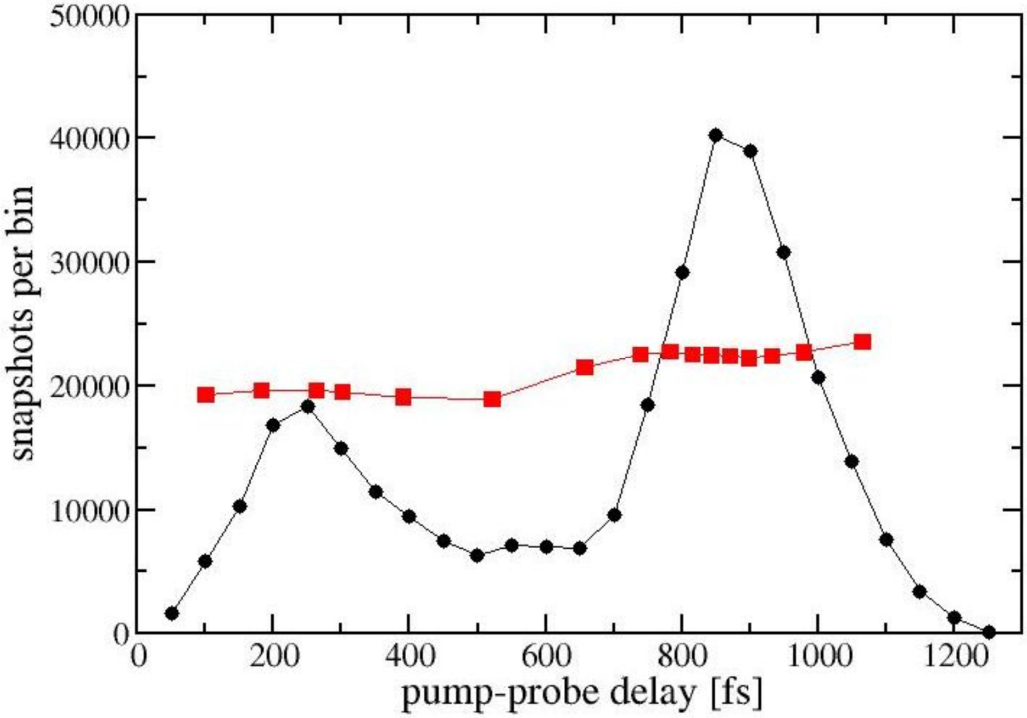

Figure S1. Snapshot density (diffraction patterns per 50 fs interval). The influence of a substantially varying number of patterns per bin on data quality is avoided when bins with approximately equal number of patterns per bin are used (e.g. red squares illustrate use of 16 bins; see Tab. S1. Unavoidably, these 16 bins are of non-uniform width in time).

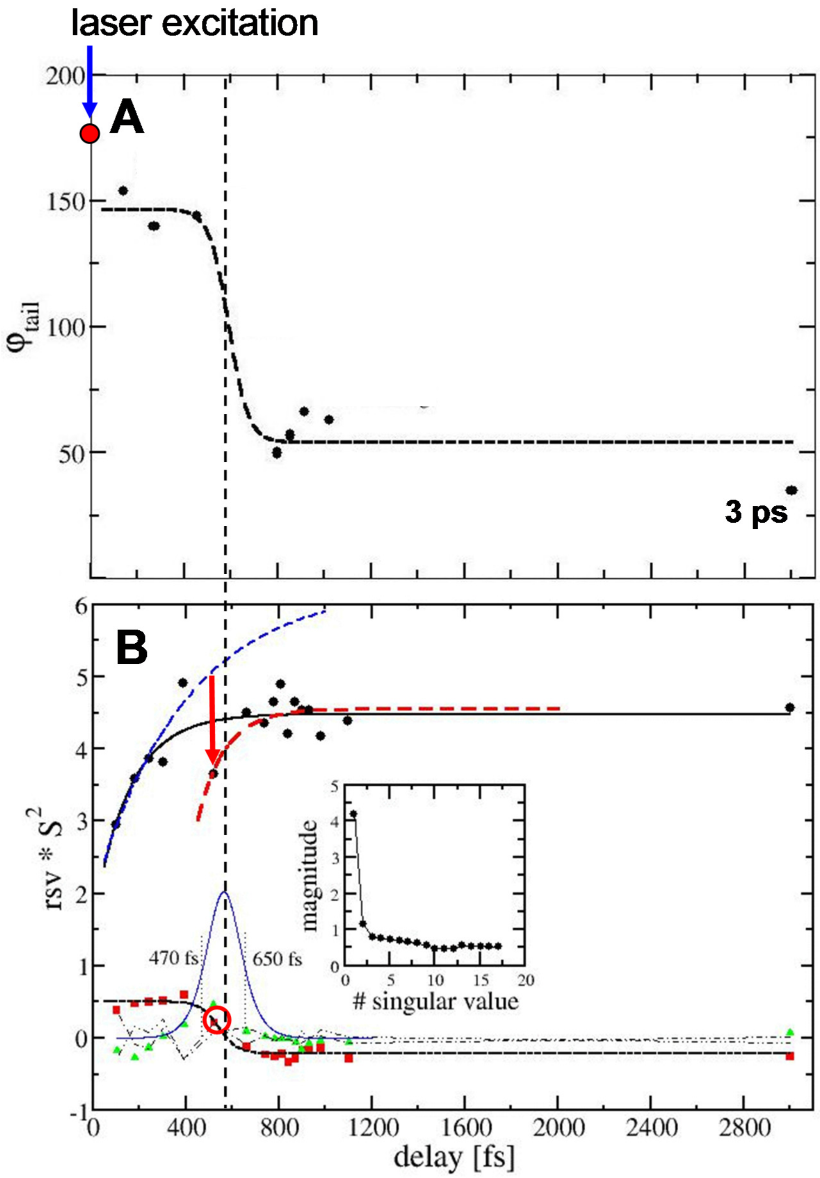

Figure S2. A. Torsional angle ϕ_{tail} from refinement at various time delays (from bins containing 40 k diffraction patterns, see also Tab. S2B and S5). Dashed line: fit by eqn. S2 with a 590 fs transition. B. Right singular vectors (rSV) from the singular value decomposition of the 17 difference electron density maps on the fs (with 20 k diffraction patterns in each bin) to 3 ps time scale. Black dots: rSV1; black line: fit with exponential (eqn. S1) with characteristic time $\tau = 155$ fs; blue and red dashed lines: fit of two separate parts of the rSV1 with exponentials. Red arrow: transition. Red squares: rSV2, dashed black line: fit by an exponential function (eqn. S2) with a 560 fs transition. Circle: time point near the assumed conical intersection. Green triangles: rSV3. The values of rSV4 and rSV5 are not significant, and displayed by thin dashed dotted and dashed double dotted lines. Blue bell-shaped curve: duration of the transition, from 470 to 650 fs. Inset: magnitude of the singular values.

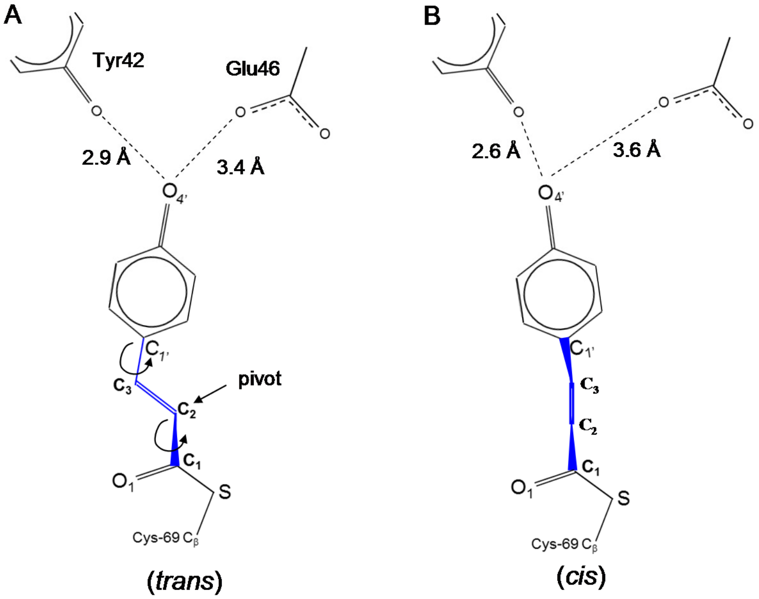

Figure S3. Schematic view of the *trans* to *cis* transition at 550 fs. The rotations can be easily understood using an educator's stick model set for chemical structures. A. PYP_{fast} structure. To produce PYP_{fast} from the reference, PYP_{ref}, grab the C_2=C_3 double bond with the left hand and the C_1-S bond with the right hand. Rotate the double bond clockwise by about 40°. The C_1-C_2 single bond points now backwards as observed, the configuration is still *trans*. Compared to the dark state, the hydrogen bonds to Glu46 and Tyr42 are elongated. To further the isomerization (and reach B), continue rotating the double bond clockwise by an additional 90° by keeping the atom C_2 location fixed. The entire head-structure pivots about (the fixed) atom C_2. Since the head cannot swing out, concerted anti-clockwise rotations about the C_1-C_2 and the C_3-C_1' single bonds are necessary to minimize the volume swept out by the atoms that move during isomerization; see arrows in A. B. PYP_{slow} structure (800-1200 fs), *cis*. The hydrogen bond to Glu46 is broken (head displacement exaggerated for clarity).

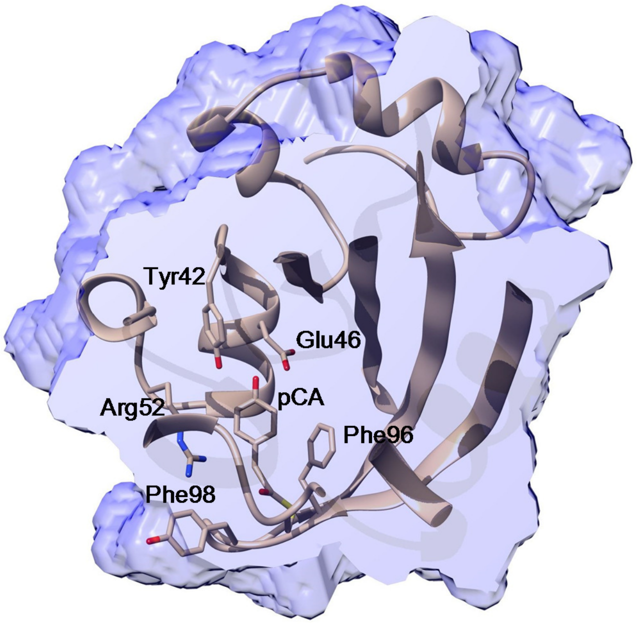

Figure S4. The solvent accessible surface (blue) of PYP_{3ps}.

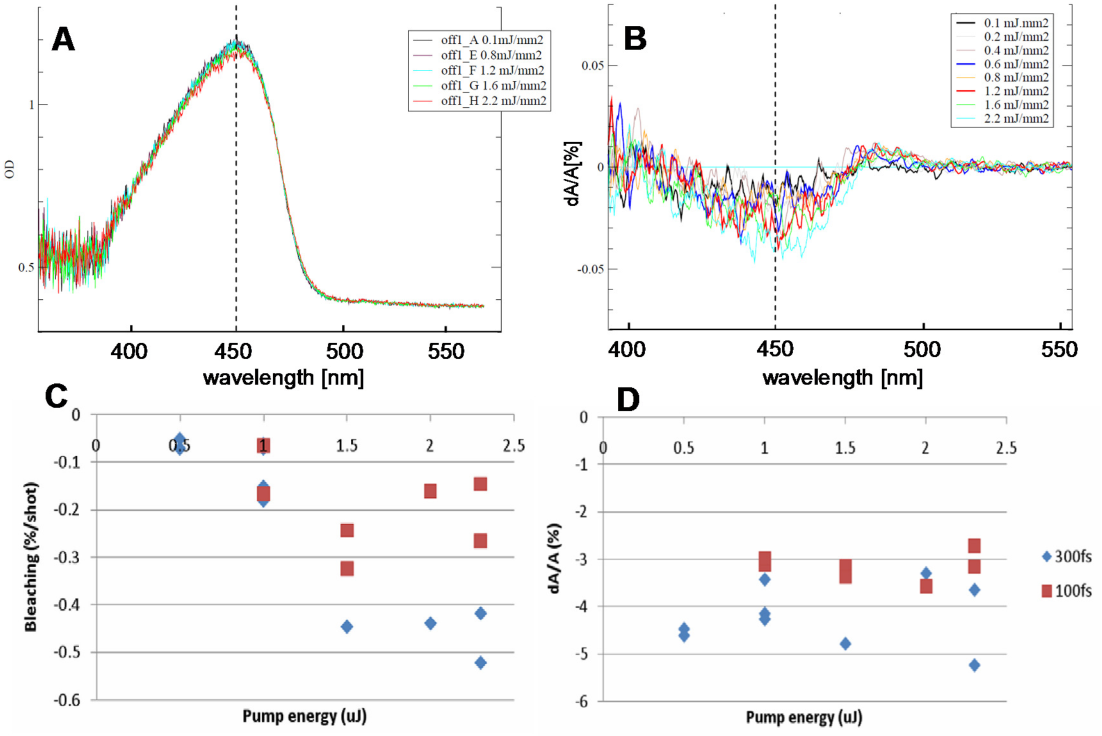

Figure S5. Entry into the photocycle in PYP crystals as evident by optical absorption changes initiated by 900 fs (A-B), 300 fs, and 100fs (C-D) laser pulses. Pump-probe delay 180µs for A-B, 1 ms for C-D. A. PYP absorption spectra of the dark state, following a sequence of 10 pump-probe cycles with 900 fs pulses at increasing laser pulse energy densities (shown in the legend). Irreversible bleaching (damage), as evident by the reduced OD of the dark state, occurs at 2.2mJ/mm^2. B. Light-dark difference absorption spectra at various laser pulse energy densities. Spectra are recorded by accumulating 10 pump-probe cycles. Extent of (reversible) bleach at 450 nm is roughly proportional to number of molecules in photocycle. At 1.2 mJ/mm^2 about 5% of molecules can be pumped into the photocycle. C. Permanent single-shot photo-bleaching (damage) measured after 100 fs (red squares) and 300 fs (blue diamonds) laser pulses of various energies (spot size 80 µm). D. Extent of reaction initiation with 100 fs and 300 fs laser pulses measured as the pB concentration at 1ms as the reversible $\Delta A_{450nm}/A_{450nm}$. 100 fs laser pulses with 2 µJ (energy density: 400 µJ/mm^2) result in up to 6% reaction initiation with small permanent damage.

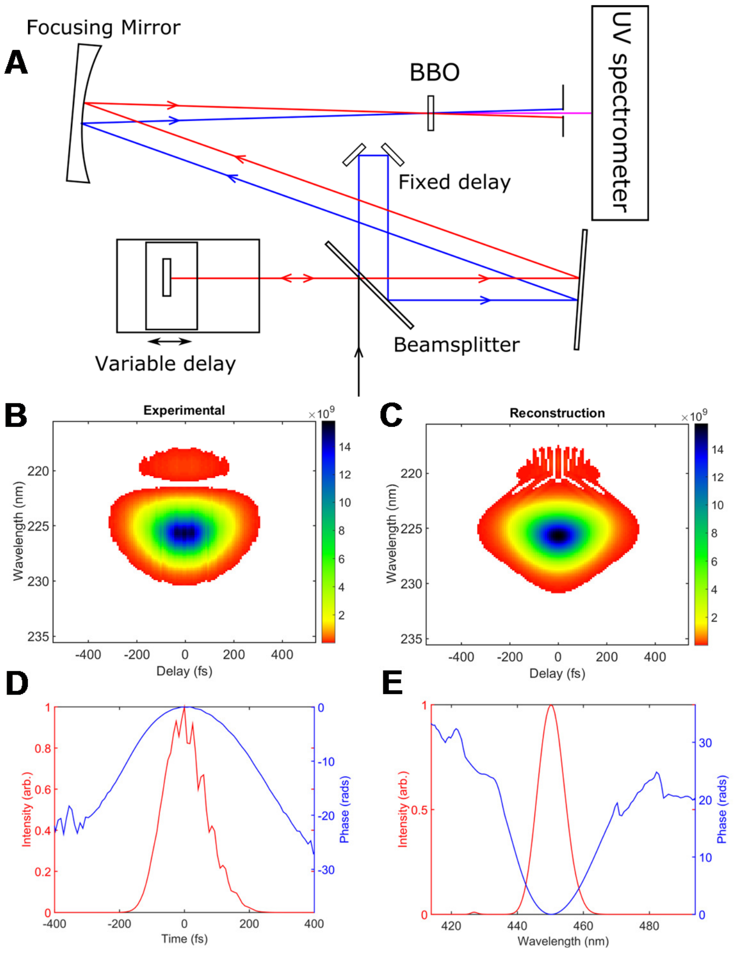

Figure S6. A. A diagram of the SHG-FROG used to characterize the 450nm femtosecond pulses incident on PYP crystals. The incoming pulse (black) is split into two replicas that travel down individual paths (shown in blue and red for clarity) until they are overlapped in a space and time in the 20 μm thin BBO crystal. The resulting FROG signal (pink) is measured using the UV spectrometer. B. The experimentally measured FROG traces for the 140 fs stretched pulse. C. Reconstructed FROG traces. The "G error" for the fitting was <1%. The high order structure seen at the top of the reconstruction that is not seen in the experimental data is the result of fluctuations in the shot-to-shot pulse shape. This is commonly seen in multi-shot FROG measurements and does not greatly impact the recovered pulse length or phase. D-E. FROG reconstruction of the temporal and the spectral intensity (red) of the reconstructed pulse incident on the PYP microcrystals with the retrieved phase indicated (blue). High order time-structure is a reconstruction artifact due to beam intensity instability (*85, 86*). The pulses were found to be 140±5 fs long with a GDD of ≈1000fs^2 and TOD ≈+1300fs^3.

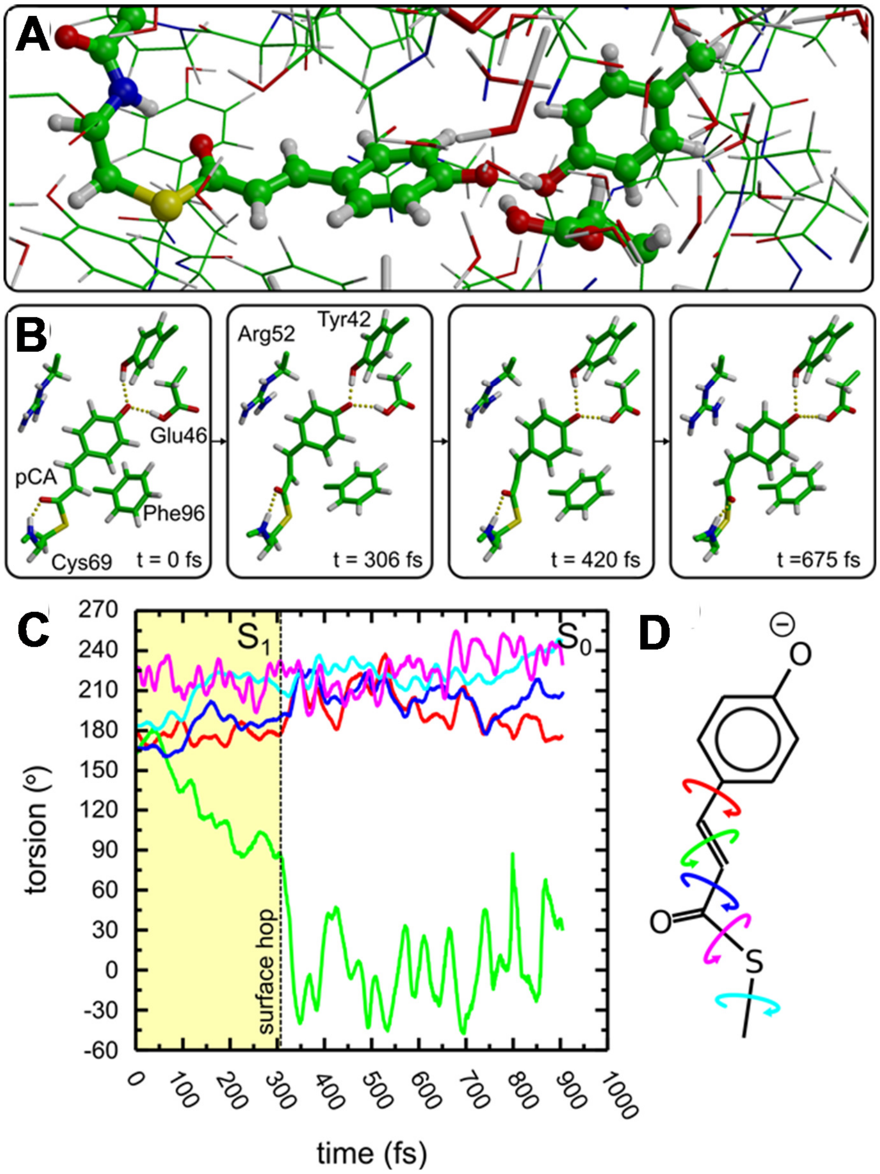

Figure S7. A. PYP configurations along the QM/MM trajectory. The atoms included in the QM region are shown in ball-and-stick representation and modeled at the CASSCF(12,11)/cc-pVDZ level of *ab initio* theory. The rest of the system, consisting of the protein, water, Cl^- and Na^+ counter ions (most of which is not shown here) are modeled with the Amber03 force field. B. Snapshots from a QM/MM trajectory after photo-excitation at t = 0 fs (Tab. S4, trajectory a). C. Torsional angles as a function of time in this trajectory. Left yellow shaded region, dynamics on the excited state potential energy surface. Vertical dashed line (surface hop): seam that separates excited state structural dynamics (left) from ground state dynamics (right). D. Color code for the torsional angles of the pCA chromophore in C.

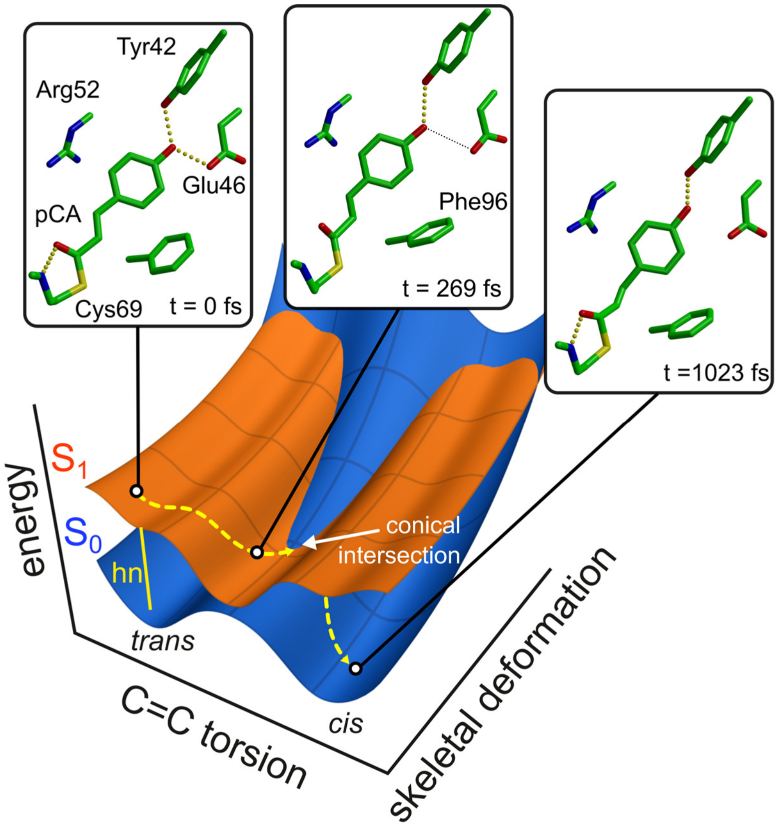

Figure S8. Transition through conical intersection as conceived from theoretical consideration (lower scheme) and viewed from the perspective of the TR-SFX experiment (structures above).

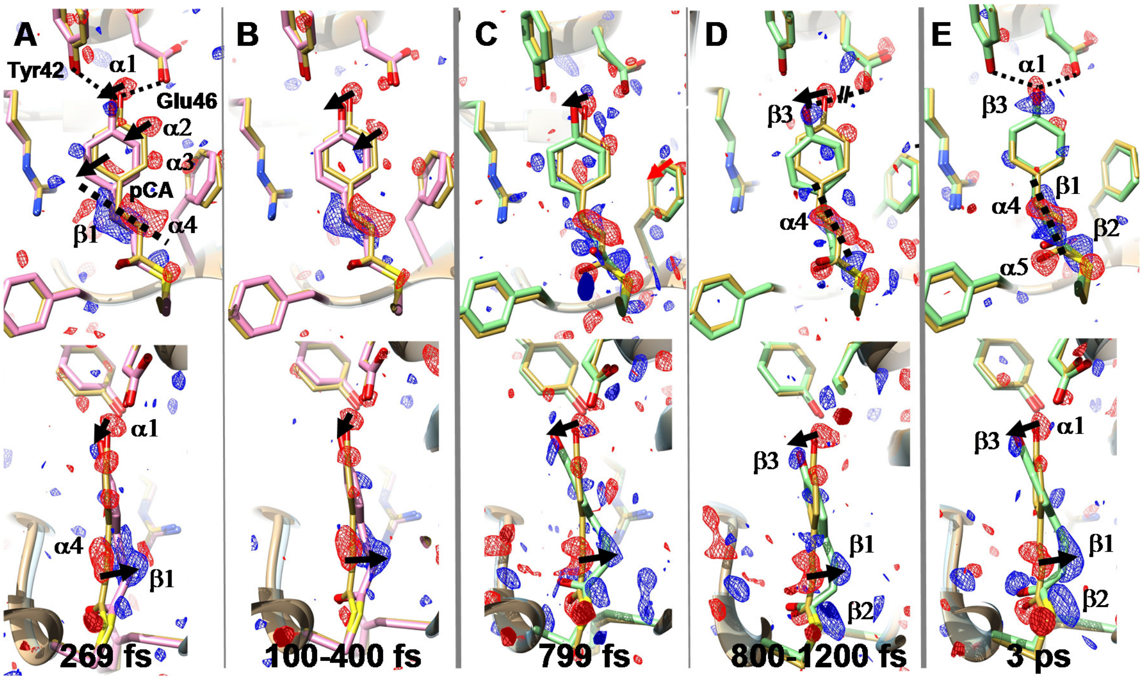

Figure S9. *Trans* to *Cis* isomerization in PYP. Direct comparison of difference maps and structures of individual time-points determined from 40,000 diffraction patterns with those determined from averaging diffraction pattern in larger time-bins (compare Tab. S1 B-C). The 269 fs, 799 fs and 3 ps delays (panels A,C and E) delays are also shown in Fig. 2 in the main text. Weighted DED maps in red (-3 σ) and blue (3σ); front (upper) and side view (lower). The reference, dark structure is shown in yellow throughout; structures before the transition and on the electronic excited state PES are shown in pink; structures after the transition and on the electronic ground state PES are shown in green. Important negative difference density features are denoted α, positive features as β. Pronounced structural changes are marked by arrows. A. Representative time-delay (269 fs) before the transition; some important residues are marked. Dotted lines: hydrogen bonds of the ring hydroxyl to Glu46 and Tyr42. B. Chromophore configuration (PYP_{fast}) by averaging 100 fs to 400 fs pump-probe delays. C. Representative time delay (799 fs) after the transition. D. Structure PYP_{slow} on longer fs times obtained by averaging the 800 fs to 1200 fs pump-probe delays. E. 3 ps chromophore configuration. Dashed lines in A, D and E: direction of feature β1.

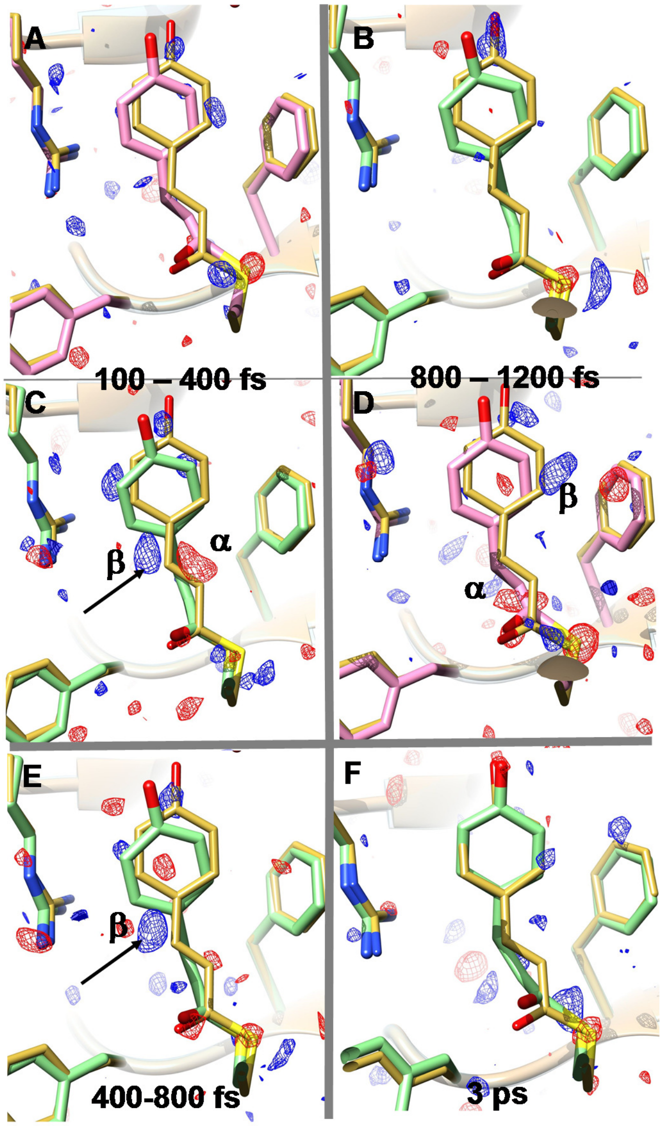

Figure S10. Difference-difference maps (residual maps): Calculated $|F^{calc}(t)|$-$|F^{calc}(dark)|$ difference maps were subtracted from the observed $|F^{obs}(t)|$-$|F^{obs}(dark)|$ difference maps. Pink: PYP_{fast}; green: PYP_{slow} and PYP_{3ps}; yellow: PYP_{ref}. Residual features (blue: positive, red negative) on the +/-3 σ level. A and B. Fast and slow fs time scale, residual maps using the correct, refined models that correspond to the time-scales, twisted-*trans* for A, and *near*-cis for B. C and D. Residual maps using interchanged, deliberately incorrect models, near-*cis* for C and twisted-*trans* for D. The chromophore tail is much cleaner in A and B, but strong residual features denoted α and β in C and D indicate mismatch. Note: remaining features near the sulfur emerge from its strong electron density; its position is difficult to model exactly. E. Data binned from 400-800 fs across the transition. Feature β shows some mixing-in of the PYP_{fast} structure in this time range. F. residual map at 3 ps time delay.

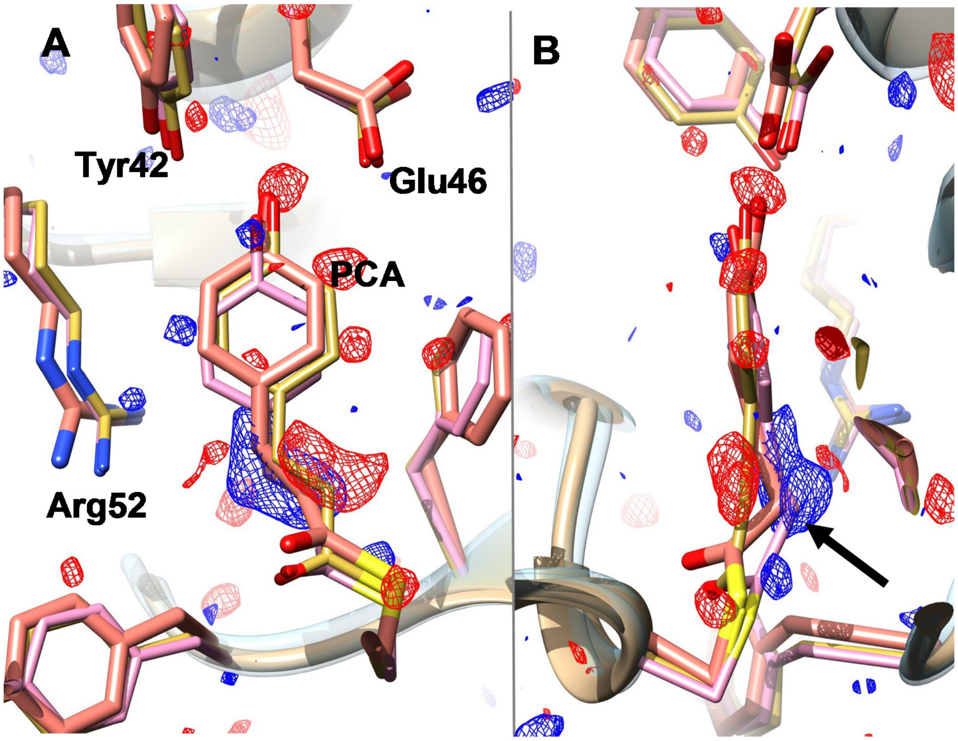

Figure S11. PYP$_{ref}$ (yellow), PYP$_{fs,fast}$ (pink) and the theoretical PYP model from QM/MM simulations (orange) overlaid on the 269 fs difference map (red/blue -3σ/4σ). A. front view, B. side view. Nearby amino acid residues are marked in A. Arrow in B: similar chromophore tail displacements for the observed and theoretical PYP structures.

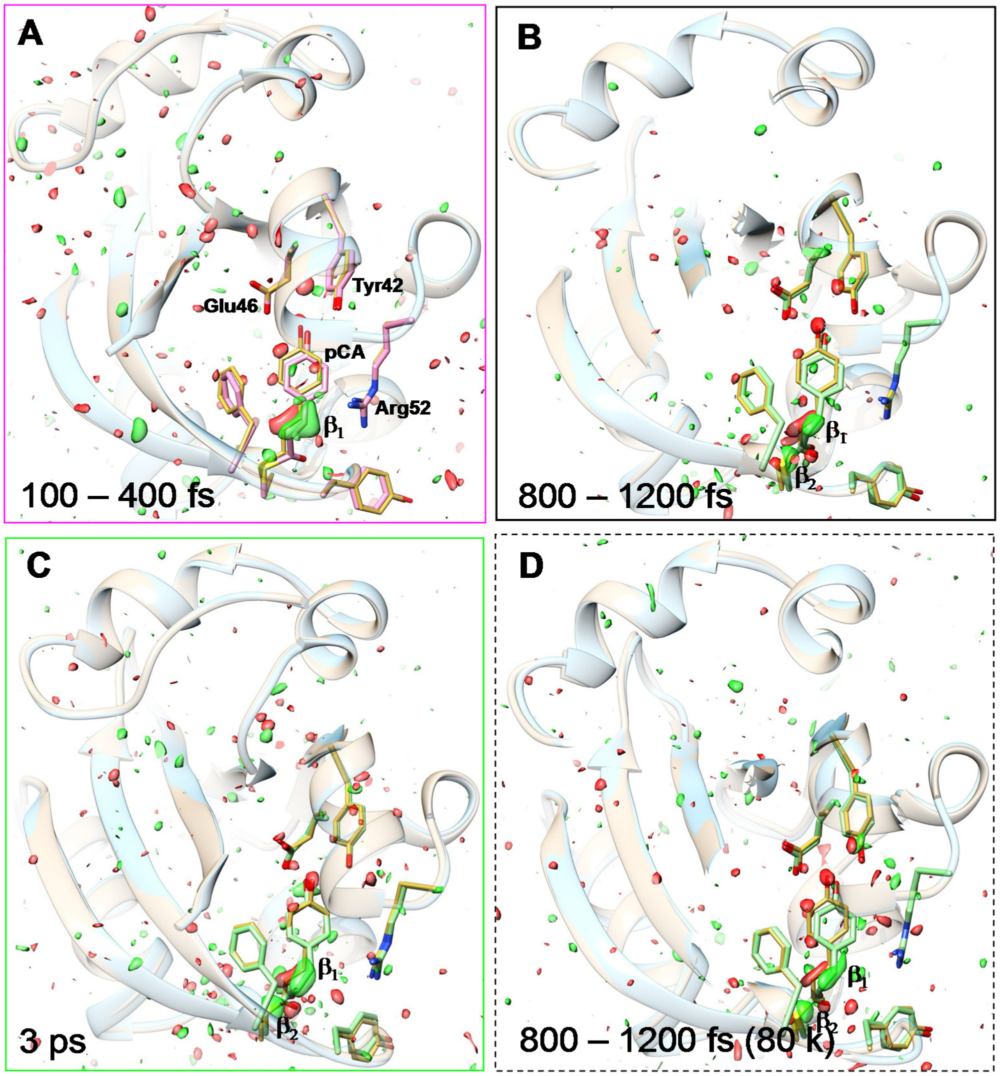

Figure S12. Full view of the DED maps (contour: red/green $-3\sigma/3\sigma$) at various time-ranges. The maps are overlaid on PYP_{ref} (yellow) and the refined structures. Contrary to all other figures that depict PYP structures, the view is from the opposite (back) of the chromophore, hence the Arg52 is on the right. This orientation allows for a detailed view of the positive feature β_1 which indicates the configuration of the chromophore and the strong feature on the Cys69 sulfur (β_2) that is also associated with the *cis* configuration. A. On the fast time scale, feature β_1 is strongly bent, β_2 is absent. The DED map is interpreted with a *trans* configuration (structure in pink). B. The slow time range, feature β_1 is aligned along the tail axis, which indicates a *cis* configuration (structure in green). C. At the 3 ps delay feature β_1 is similar to B (structure also in green). D. Consistency check by randomly selecting ~80,000 snapshots from the 157,000 snapshots in the bin. DED map with features β_1 and β_2 and structure (green) essentially the same as in B.

Table S1. TR-SFX data statistics. Resolution 1.6 Å; data in the highest resolution bin (1.6 - 1.67 Å) in brackets. A. Statistics of the data sorted into time bins with 32,690 snapshots with Bragg reflections (hits)/bin (approximately 20,000 indexed snapshots/bin). Times shown are the average of the time stamps in each bin and their standard deviation. B. Data statistics of bins with 65,380 snapshots/bin (approximately 40,000 indexed snapshots/bin). C. Statistics of the individual -1ps, 3 ps and 200 ns time points and when snapshots with time-stamps 100 – 400 fs and 800 – 1200 fs are combined.

A

Time	**# indexed**	**R-split**	**CC***	**Completeness**	**Multiplicity**
100.8 ± 43 fs	19313	12.84 (37.42)	0.994 (0.926)	99.84 (100)	342.76 (25.2)
182.8 ± 16 fs	19659	12.58 (38.60)	0.994 (0.925)	99.84 (100)	348.41 (26.3)
236.3 ± 16 fs	19647	12.93 (41.08)	0.994 (0.896)	100 (100)	341.26 (26.0)
301.5 ± 22 fs	19480	13.19 (36.77)	0.993 (0.933)	99.76 (100)	330.86 (25.3)
390.7 ± 31 fs	19090	13.70 (43.08)	0.993 (0.904)	99.92 (100)	312.83 (22.2)
521.0 ± 38 fs	18905	14.30 (35.20)	0.992 (0.925)	99.97 (100)	295.09 (30.5)
657.5 ± 37 fs	21500	11.83 (25.12)	0.994 (0.968)	99.84 (100)	409.97 (59.1)
739.5 ± 15 fs	22554	10.99 (21.89)	0.995 (0.978)	99.76 (100)	459.67 (68.2)
782.4 ± 11 fs	22816	10.95 (23.76)	0.995 (0.969)	99.84 (100)	468.66 (69.0)
814.9 ± 9 fs	22560	10.83 (23.70)	0.995 (0.972)	100 (100)	467.46 (64.6)
842.8 ± 8 fs	22507	10.97 (24.63)	0.995 (0.962)	99.84 (100)	463.5 (63.0)

870.1 ± 8 fs	22416	10.76 (24.18)	0.995 (0.971)	99.6 (100)	465.45 (60.0)
898.8 ± 9 fs	22266	10.54 (23.59)	0.996 (0.972)	99.84 (100)	466.38 (61.8)
931.7 ± 11 fs	22409	10.49 (21.76)	0.996 (0.976)	100 (100)	472.31 (64.4)
978.4 ± 16 fs	22732	10.44 (23.46)	0.995 (0.964)	99.84 (100)	478.35 (67.2)
1064.8 ± 45 fs	23605	10.43 (20.94)	0.995 (0.975)	99.92 (100)	501.62 (75.9)

B

Time	**# indexed**	**R-split [%]**	**CC***	**Completeness**	**Multiplicity**
142 fs	38606	9.01 (26.05)	0.997 (0.962)	99.92 (100)	714.75 (48.5)
269 fs	38786	9.16 (26.08)	0.997 (0.959)	100 (100)	695.25 (49.6)
455 fs	37563	9.86 (26.58)	0.996 (0.957)	99.84 (100)	637.31 (57.7)
699 fs	43617	7.53 (16.94)	0.998 (0.984)	99.92 (100)	931.65 (124.9)
799 fs	44892	7.57 (19.84)	0.998 (0.974)	99.84 (100)	961.51 (121.1)
856 fs	44470	7.61 (17.60)	0.997 (0.983)	99.92 (100)	955.96 (112.9)
915 fs	44180	7.58 (18.75)	0.998 (0.981)	99.84 (100)	927.25 (106.3)
1023 fs	45880	7.53 (17.19)	0.998 (0.978)	99.76 (100)	971.3 (123.7)

C

Time	**# indexed**	**R-split [%]**	**CC***	**Completeness**	**Multiplicity**
Reference (-1 ps)	82214	7.69 (14.83)	0.998 (0.987)	99.93 (100)	991.51 (22.1)
100 – 400 fs	81327	6.13 (18.13)	0.998 (0.981)	100 (100)	1546.81 (115.6)
800 – 1200 fs	157082	4.03 (9.11)	0.999 (0.989)	100 (100)	3322.0 (145.9)
3 ps	76411	5.43 (14.36)	0.999 (0.989)	100 (100)	1685.8 (145.9)
200 ns	102790	5.02 (12.04)	0.998 (0.993)	99.9 (100)	2287.0 (244.2)

Table S2. Difference maps and refinement for selected structures.

Structure	**Dark**	**100 - 400fs**	**800 – 1200 fs**	**3 ps**	**200 ns**
signal +/- (sigma)[a]		6.5/6.9	5.9/8.0	7.38/8.98	18.1/18.2
R_{cryst}/R_{free}	15.5/18.2	20.6/26.1	18.5/23.9	20.6/26.0	28.9/37.5
completeness	98.5	99.0	98.9	98.9	98.9
rmsd bonds d[Å]	0.020	0.028	0.020	0.026	0.019
rmsd angles [°]	2.0	2.6	1.97	2.7	2.0
ϕ_{tail}	170	140	53	38	3/-8

[a] max signal identified in weighted difference maps in multiples of the noise level.

Table S3. Torsional angles and distances from structural refinement at various, individual time delays.

Time Delay [fs]	**142**	**269**	**455**	**699**	**799**	**856**	**915**	**1023**	**3ps**
C1-C2=C3-C1’ (ϕ_{tail})	154	140	144	na[a]	50	57	66	63	35
O1-C1-C2=C3	20	-7	15	na	36	23	32	43	30
CB-S-C1-C2	-135	-166	-154	na	-152	-152	-157	-165	-137
pCA-$O_{4'}$ - Glu46-O_{ε}	2.61	3.46	3.49	na	3.2	3.36	3.62	3.3	2.94

[a] refinement not successful presumably due to the existence of a mixture of molecules relaxing to *cis* towards the photocycle and those relaxing back to the reference state. The time course of the ϕ_{tail} in the 8 fs bins can be fit by eqn. S2 with a transition time of 590 fs, see Fig. S2A.

Table S4. Global structural changes [Å] as measured by averaging the distances between c_α atoms of equivalent residues.

Time Scale		**0**	**100 to 400 fs**	**800 to 1200 fs**	**few ps**	**100 ps to 1 ns**	**μs**
		PYP$_{\text{dark}}$	PYP$_{\text{fast}}$	PYP$_{\text{slow}}$	PYP$_{\text{3ps}}$	pR0/I$_{\text{T}}$	pR
0	PYP$_{\text{dark}}$	**0**					
100 to 400 fs	PYP$_{\text{fast,}}$	0.20 (0.09)	**0**				
800 to 1000 fs	PYP$_{\text{slow}}$	0.19 (0.09)	0.23 (0.11)	**0**			
few ps	PYP$_{\text{3ps}}$	0.24 (0.10)	0.26 (0.13)	0.25 (0.13)	**0**		
100 ps to 1 ns	pR0/IT	0.19/0.13 (0.15/0.10)	0.27/0.22 (0.14/0.11)	0.23/21 (0.14/0.11)	0.26/0.25 (0.13/0.12)	**0.15 (0.08)**[a]	
μs	pR	0.13 (0.09)	0.23 (0.12)	0.20 (0.1)	0.24 (0.11)	0.17/0.16 (0.12/0.09)	**0**
ms	pB	0.17 (0.12)	0.25 (0.13)	0.24 (0.14)	0.28 (0.13)	0.19/0.15 (0.10/0.08)	0.18 (0.12)

[a] distances between pR0 and I$_{\text{T}}$

Table S5. Excited state lifetimes (2rd column), and products (3th column) in the excited state QM/MM trajectories.

trajectory	**S_1 lifetime**	**outcome**
a	311 fs	*cis*
b	221 fs	*trans*
c	456 fs	*trans*
	<329 fs>	